RSC Advances

PAPER

View Article Online
View Journal | View Issue

Cite this: *RSC Adv.*, 2019, **9**, 7189

Simultaneous bifunctional application of solid-state lighting and ratiometric optical thermometer based on double perovskite $LiLaMgWO_6:Er^{3+}$ thermochromic phosphors

Weiguang Ran,[a] Hyeon Mi Noh,[a] Sung Heum Park,[a] Bo Ram Lee,[a] Jung Hwan Kim,[a] Jung Hyun Jeong,*[a] Jinsheng Shi[b] and Guangzeng Liu[cd]

Realization of simultaneous, efficient bifunctional application of thermochromic phosphors on light emitting diodes (LEDs) and as ratiometric thermometers is significant. Herein, doped Er^{3+} ions are introduced as an activator into double perovskite $LiLaMgWO_6$ host lattice. The developed phosphors can be efficiently excited by a near-ultraviolet LED chip and show bright green emission, mainly at 527 and 543 nm, as well as very low thermal quenching. Their chemical stability is studied, demonstrating excellent application potentials. Furthermore, the temperature sensing properties of $LiLaMgWO_6:0.01Er^{3+}$ were analyzed in the wide range of 303–483 K and show a good exponential relationship between ratiometric intensity and temperature ($R^2 > 0.999$), as well as high sensitivity (2.24% K^{-1}). Such a system not only optimizes the performance in solid light emitting but also provides an excellent platform for designing high-sensitivity optical thermometry.

Received 13th December 2018
Accepted 14th February 2019

DOI: 10.1039/c8ra10242b

rsc.li/rsc-advances

Introduction

Designing and developing multiple advanced applications based on one functional material are active subjects currently and have compelled scientists to explore more novel materials with high performance and stability through efficient synthetic strategies.[1,2] Among the advanced applications, fluorescence thermometers have attracted much attention because they provide both high spatial and temperature resolution with noninvasive detection.[3–5] Another case is pc-LED devices, in which the most promising candidate is the hybrid tricolor (blue, green and red) phosphors pumped by a near-violet (NUV) LED chip.[6,7] Rational design of efficient bifunctional materials with high performance and stability for both pc-LEDs and the ratiometric optical thermometer is critical and urgently required for Scientific Research and Development, as well as technological applications.

As is known, temperature-sensitive thermally coupled energy levels (TCELs) transport electrons from the low-energy level to the high-energy level and eventually enhances the short-wavelength emission of light at high temperatures. Higher sensitivity of TCELs means higher efficiency of heat-to-light conversion. Increasing the sensitivity of the thermally coupled energy levels is expected to reduce the thermal quenching effect of fluorescence. At the same time, thermally coupled energy levels with higher sensitivity are likely to be used in high-performance optical temperature sensors. Therefore, finding materials with ultra-sensitive thermally coupled energy levels is the key for application in the fields of pc-LED and optical temperature sensors.

Many pioneers' works have suggested that the doping of lanthanide ions represents an effective way to generate superior active sites for light emission and thermometry. For example, $RbLi(Li_3SiO_4)_2$ doped with Eu^{2+} ions was developed to deliver green emission at 530 nm with a narrow full width at half maximum of 42 nm and very low thermal quenching, while its chemical stability requires improvement.[8] 2D LaPOM@MOFs coordination polymers doped with Eu^{3+}/Tb^{3+} and Dy^{3+} ions were prepared for ratiometric optical temperature sensing.[9] But making the advantages of the support more effective for optimal combination of these two advanced applications remains a challenge.

Generally, the effectiveness of the doping is mainly dependent on the interaction between host and guests.[10,11] Thus, the applications of ratiometric temperature sensors and LEDs are dependent on the chemical and crystal state of the active centers in the host material. Double perovskites with the formula of $AA'BB'X_6$ ($X =$ oxygen, halogen) possess excellent

---

[a] *Department of Physics, Pukyong National University, Busan 608-737, South Korea. E-mail: jhjeong@pknu.ac.kr*

[b] *Department of Chemistry and Pharmaceutical Science, Qingdao Agricultural University, Qingdao 266109, People's Republic of China*

[c] *State Key Laboratory of Crystal Materials, Shandong University, Jinan 250100, PR China*

[d] *College of Chemistry and Chemical Engineering, Qilu Normal University, Jinan, 250013, PR China*

performance in various fields as a result of their distinct electronic structures.[12–14] The structure of double perovskite matrix varies with the different A(B) and A′(B′) cation pairs, which can effectively modify the electronic structure, thereby optimizing the performance.[15,16] For example, Mitzi and co-workers provided good bandgap engineering of double perovskite $Cs_2AgBiBr_6$ by ion doping for photovoltaics.[17] It is expected that the unique structure of double perovskite can serve as a capable platform for synchronously realizing bifunctional performances of LED device and ratiometric optical thermometer.

Motivated by the above discussion, herein, double perovskite $LiLaMgWO_6$ was used as a representative host to simultaneously realize bifunctional application for both fluorescence thermometers and LED devices. Benefiting from the synergistic effects between the active sites of Er^{3+} ions and the host lattice, the constructed Er^{3+}-activated $LiLaMgWO_6$ phosphors can be used in pc-LED illumination and optical temperature sensors. Additionally, the phosphors have excellent thermal and chemical stability. Undoubtedly, this work promotes the development of cost-effective bifunctional materials for applications in fluorescence thermometers and LED devices.

Experimental section

Materials and methods

A series of $LiLaMgWO_6$:x Er^{3+} (with $x = 0$, 0.005, 0.01, 0.015, 0.02, 0.025, 0.03, 0.04, and 0.05) phosphors were synthesized by the high-temperature solid-state method. Stoichiometric amounts of Li_2CO_3 (AR, 99.9%), WO_3 (Aladdin reagent, 99.9%), MgO (AR, 99%), La_2O_3 (Aladdin reagent, 99.99%), and Er_2O_3 (Sinopharm Chemical Reagent, 99.999%) were mixed thoroughly in a planetary ball mill for 10 h and preheated at 800 °C for 6 h. Subsequently, the products were removed from the muffle furnace, allowed to cool, finely ground, and then sintered in air for 12 h at 1100 °C. Finally, the products were cooled to room temperature and ground to yield powders.

Characterization

X-ray diffraction (XRD) measurement was carried out by an X'Pert^3 powder diffractometer with Cu $K_{\alpha1}$ radiation ($\lambda = 0.1540598$ nm). The morphological and structural behaviors of the final compounds were examined utilizing a field-emission scanning electron microscope (FE-SEM; LEO SUPRA 5) equipped with an energy dispersive X-ray (EDX) spectrometer and a transmission electron microscope (TEM) (JEM-2100F, JEOL). X-ray photoelectron spectroscopy (XPS) measurements were performed on an ESCALAB MKII X-ray photoelectron spectrometer by monochromatic Al Kα X-rays. UV-visible diffuse reflectance spectra (DRS, with $BaSO_4$ as an internal reference sample) were recorded from dry-pressed disk samples using a V-670 (JASCO) UV-vis spectrophotometer equipped with an integrating sphere assembly. The room-temperature photoluminescence spectra were checked by a Photon Technology International (PTI) spectrofluorometer set-up equipped with a 60 W Xe-arc lamp. The lifetime was measured using a phosphorimeter attached to the primary system with a Xe-flash lamp (25 W). The temperature dependent PLE and PL spectra of the as-prepared phosphors were detected using a spectrofluorometer (Scinco FluroMate FS-2) with a xenon lamp as the light source. The temperature range from 303 to 483 K was realized using a thermocouple (NOVA ST540). The quantum efficiency (QE) was measured using a fluorescence spectrometer (JASCO FP-8500, JAPAN). The multi-channel spectroradiometer (OL 770) was employed to detect the electroluminescence (EL) properties of the fabricated LED devices under a forward bias current (*i.e.* 100 mA).

Results and discussion

Functional materials with perovskite structure have been widely used in many fields, as a result of its unique crystal structure.[18–21] $LiLaMgWO_6$ served as host lattice to prepare the Er^{3+}-activated thermochromic phosphors for bifunctional applications in WLEDs and as ratiometric optical thermometers. The investigated $LiLaMgWO_6$ is a double perovskite sample, in which Mg^{2+} and W^{6+} ions alternate on the perovskite B-sites (Fig. 1a).

Physical and chemical properties characterizations

Characterizations of the physiochemical properties were performed to detect the structure and phase information of the samples. XRD measurements were carried out first, as shown in Fig. 1b. The diffraction peaks can be well matched with the phases of $NaLaMgWO_6$ (JCPDS no. 37-0243). In comparison with $LiLaMgWO_6$ host, all the doped phosphors give similar XRD peaks (Fig. 1b). As the concentration of Er^{3+} increases, no obvious shift is observed for the dominant characteristic diffraction peak (020) of the system as a consequence of the similar radii of Er^{3+} and La^{3+} ions in the same coordination environment. The refinements of lattice parameters for pristine and doped phosphors are given in the inset of Fig. 1c. These results indicated that the introduced Er^{3+} ions are located at the position of La^{3+} sites.

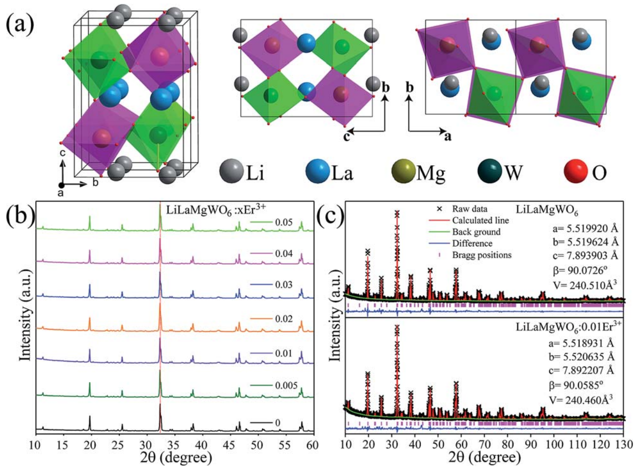

Fig. 1 (a) Schematic crystal structure of $LiLaMgWO_6$. (b) XRD patterns of $LiLaMgWO_6$:x Er^{3+} with $x = 0$, 0.005, 0.01, 0.02, 0.03, 0.04, and 0.05. (c) Rietveld refinement XRD patterns of $LiLaMgWO_6$ host and $0.01Er^{3+}$-activated $LiLaMgWO_6$ phosphor, respectively.

To obtain direct information about texture and morphology of the samples, SEM and TEM analyses were carried out and typical images are shown in Fig. 2. Well-dispersed spherical particles can be seen in Fig. 2a and b. Additionally, the element mapping results indicated that the elements in the Er^{3+}-activated phosphors were uniformly distributed, as shown in Fig. 2c. This is evidence for successful incorporation of Er^{3+} into the host lattice. TEM and HRTEM were then performed for information about the phosphors, as shown in Fig. 2d and e, respectively. The sample presents obvious lattice fringes with measured spacing of 0.276 nm, which is in good agreement with the (020) facet of the host. In addition, the SAED pattern shows a dot feature, indicating the single crystalline nature of our prepared samples (Fig. 2f).

To further confirm the chemical structure of the samples, the existence of Er^{3+} doping can be verified utilizing XPS (Fig. 2g), which is very sensitive to the surface and subsurface chemical states. We carried out the high-resolution XPS analysis of Li (inset in Fig. 2g). In Li 1s region, one peak centred at 55.0 eV can be found. DRS was carried out to study the light absorption capacities of the samples. As shown in Fig. 2h, in the case of the pure host, it displays strong and flat absorption bands in the NUV region, which may be due to the CTB of O^{2-} to W^{6+} (250–350 nm). This result suggests that doping can expand the light absorption range of the host. The sharp absorption peaks of doped phosphor appear in the visible region because of the 4f transitions of Er^{3+} ions,[22] which matches well with the excitation spectra.

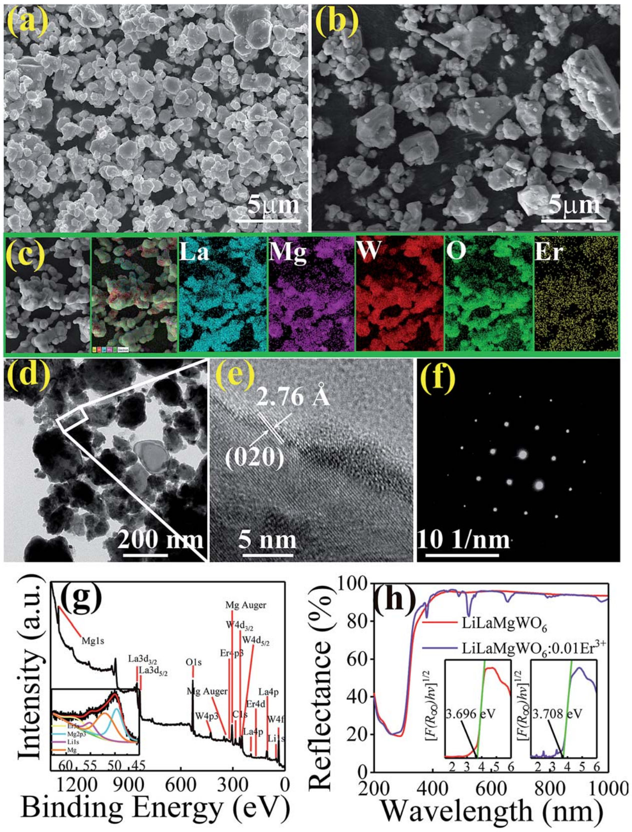

Fig. 2 (a and b) FESEM of the host and Er^{3+}-activated $LiLaMgWO_6$ phosphor samples, respectively. (c) SEM element mapping of related phosphors. (d) TEM and (e) HRTEM images of the Er^{3+}-activated $LiLaMgWO_6$ phosphor samples under study. (f) The corresponding SAED pattern of studied samples. (g) XPS analysis of the studied samples. (h) UV-vis diffuse reflectance spectra of samples.

Luminescence properties under room temperature

The excitation and emission spectra of prepared phosphors were recorded to monitor the intra-4f transitions corresponding to the Er^{3+} emission at 544 nm. According to the result in Fig. 3a, the broad excitation band between 250 and 350 nm can be assigned to the charge transfer (CT) bands of the phosphors ($O^{2-} \rightarrow W^{6+}$). The set of narrow peaks between 350 and 500 nm is characteristic of Er^{3+}. In detail, the narrow peaks at 364, 378, 407, 449 and 488 nm are assigned to transitions from the ground state of $^4I_{15/2}$ to the $^4G_{9/2}$, $^4G_{11/2}$, $^2H_{9/2}$, $^4F_{5/2}$ and $^4F_{7/2}$ transition states of Er^{3+}, respectively.

In comparison with the other peaks, the band centred at approximately 378 nm exhibited the strongest intensity, which reveals that near-ultraviolet (NUV) light was the appropriate excitation source for the studied phosphors. In detail, as the doping content increases, the intensity shows an increasing trend. The intensity value is maximum at 1% doping (inset of Fig. 3a). When exceeding this doping level, the intensity reduces slightly, with 5 mol% the lowest, which may result from the concentration quenching effect. In the PL emission spectra using a 378.25 nm excitation light, as shown in Fig. 3b, the two strong emission peaks centred at 527 and 544 nm belong to the transitions of the thermally coupled $^2H_{11/2}$ and $^4S_{3/2}$ energy levels, respectively, to the ground state ($^4I_{15/2}$). In addition, a weak red emission corresponding to the $^4F_{9/2} \rightarrow {}^4I_{15/2}$ transition is shown. Owing to their efficient light emission, the studied materials emit strong green light when pumped with NUV light. The tendency of doping concentration-dependent intensity of emission spectra is similar to that of the excitation spectra.

Furthermore, we explore the doping concentration-dependent quenching mechanism for our developed phosphors. First, the critical distance (R_c) of the activators was calculated:

$$R_c = 2\left(\frac{3V}{4\pi x_c Z}\right)^{\frac{1}{3}}. \quad (1)$$

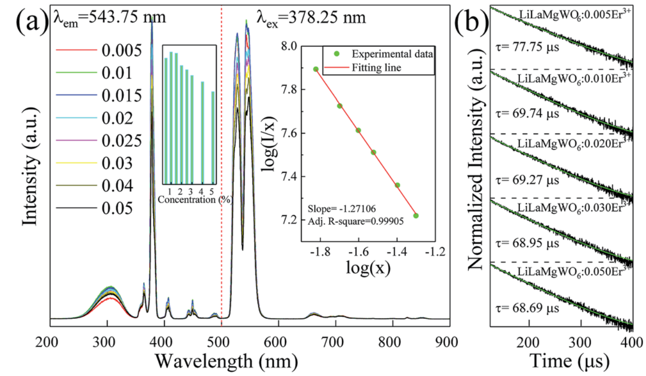

Fig. 3 (a) Excitation (λ_{em} = 543.75 nm) and emission (λ_{ex} = 378.25 nm) spectra of $LiLaMgWO_6$:xEr^{3+} samples as indicated. (b) Decay curves of the $^4S_{3/2}$ level for $LiLaMgWO_6$:xEr^{3+} particles.

In the above equation, the parameters V, x_c, and Z represent the volume of the unit cell, optimal doping content and the number of cation sites in the unit cell which can be occupied by Er^{3+} ions, respectively. In this study, the related values of V, x_c, and Z are 240.51 Å^3, 0.01 and 2, respectively and we can obtain the value of R_c (28.39 Å). Based on Dexter's report,[23] the relation between the PL emission intensity and doping concentration can be expressed as:

$$\frac{I}{x} = k\left(1 + \beta(x)^{\frac{Q}{3}}\right)^{-1} \tag{2}$$

where x refers to the concentration of activator and k and β are related to the coefficients. $Q = 3$ stands for the energy transfer among the nearest neighbor ions, while Q equals 6, 8, and 10 represent the dipole–dipole, dipole–quadrupole, and quadrupole–quadrupole interactions, respectively.

Eqn (2) can be written equivalently[24] when $x > x_c$:

$$\log\left(\frac{I}{x}\right) = C - \left(\frac{Q}{3}\right)\log(x) \tag{3}$$

Here, C is a coefficient. To obtain the value of Q, the relation between $\log\left(\frac{I}{x}\right)$ *vs.* $\log(x)$ is shown in the inset of Fig. 3b. The experimental results can be fitted linearly and the slope $\left(-\frac{Q}{3}\right)$ was found to be around −1.27106. Therefore, the value of Q can be calculated as 3.81318, which is near to 3, indicating that the concentration quenching of Er^{3+} ions is dominated by the energy transfer among the nearest neighbor ions in the $LiLaMgWO_6{:}xEr^{3+}$ phosphor.

The decay curves of the phosphors under study were measured to explore the concentration quenching phenomenon of Er^{3+} emission. According to the results in Fig. 3c, all decay curves of studied phosphors can be well fitted with a first-order exponential equation. The lifetime reduces with increase of doping concentration of Er^{3+} ions. Visible differences can be detected in the PL curves, with the 5 mol% doping showing the fastest PL decay (68.69 μs) and 0.5 mol% doping the slowest (77.75 μs).

To explore the origin of light absorption of the host lattice, the band structure and density of states (DOS) were calculated. As seen from Fig. 4a, we observe that the valence band (VB) maximum and conduction band (CB) minimum are located at different points, confirming that the host lattice is an indirect band-gap semiconductor. The calculated band gap of the pure host is 3.430 eV, which is smaller than the experimental band gap of 3.696 eV, due to the well-known shortcomings of GGA.[25] Furthermore, by analyzing the projected density of states (PDOS), we can understand in depth the composition of the electronic structure. As shown in Fig. 4b, the conduction bands (CB) are formed by O_{2p} state, while the CBM is attributed dominantly to O_{2p} and W_{5d} states. Under UV light irradiation, the WO_6^{6-} group is excited as a result of the charge transfer transition from the O_{2p} states within the valence band of the host W_{5d} states in the host's conduction band.

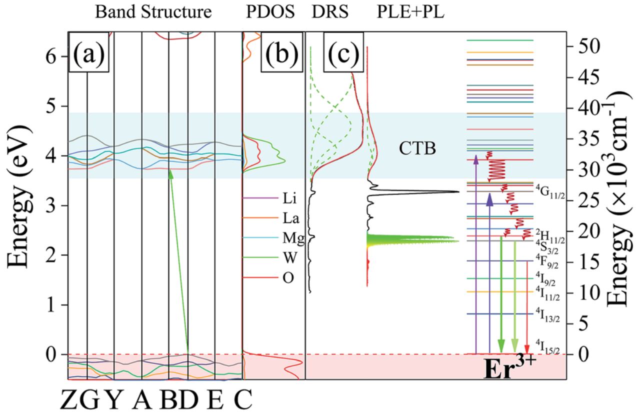

Fig. 4 DFT calculation studies of $LiLaMgWO_6$ phosphor: (a) band structure and (b) PDOS. (c) The DRS, PLE, PL, and energy level diagrams involved in the energy transfer process from CTB to Er^{3+} in $LiLaMgWO_6{:}Er^{3+}$ phosphors.

Combined with the DRS and PLE spectra, we find that the two broad bands located at 31 943 cm^{-1} and 34 327 cm^{-1} result from the strong absorption of O–W CTB. The energy level diagrams involved in the energy transfer process from the CTB to Er^{3+} in $LiLaMgWO_6$ are illustrated in Fig. 4c. Under near-UV light excitation, the electron located at the $^4I_{15/2}$ ground state level can be excited. The electron, after energy transition from the high energy level to the $^2H_{11/2}$ and $^4S_{3/2}$ states, can relax to the $^4I_{15/2}$ state, leading to green emission.

Thermal and chemical stability of developed phosphors

In general, the thermal and chemical stability of phosphor is critical for its application in solid light emitting. As shown in Fig. 5a, the overall shape and position of the emission spectra remain unchanged as the temperature is increased from 303 to 483 K. The inset shows the intensity change depending on increasing temperature. Both thermal quenching and thermal excitation are simultaneously present in the Er^{3+} doped $LiLaMgWO_6$ phosphors. Due to the presence of sensitive thermally coupled energy levels ($^2H_{11/2}$–$^4S_{3/2}$) in the $LiLaMgWO_6{:}Er^{3+}$ phosphor, more and more electrons in the $^4S_{3/2}$ energy level were excited to the $^2H_{11/2}$ energy level with the increase of temperature. Therefore, the thermal quenching rate of the long-wavelength emission from $^4S_{3/2} \rightarrow {}^4I_{15/2}$ transition in $LiLaMgWO_6{:}Er^{3+}$ phosphor was accelerated. The thermal quenching phenomenon of short wavelength emission from $^2H_{11/2} \rightarrow {}^4I_{15/2}$ transition was compensated. Therefore, the long-wavelength emission is more affected by temperature. Additionally, in quantitative analysis, the integrated emission intensity at 443 K drops only 25% compared to the initial intensity at room temperature and, even at 483 K, the integrated emission intensity remains over 60% of that at room temperature, indicating the excellent thermal stability of our developed phosphors.

Chemical stability of the phosphors was investigated in this work. Fig. 5c gives PL emission spectra of the $LiLaMgWO_6{:}0.01Er^{3+}$ phosphors before and after various water treatments. All curves have a similar position and intensity, confirming the excellent water resistance properties of our developed phosphors, as suggested by the visual behavior of

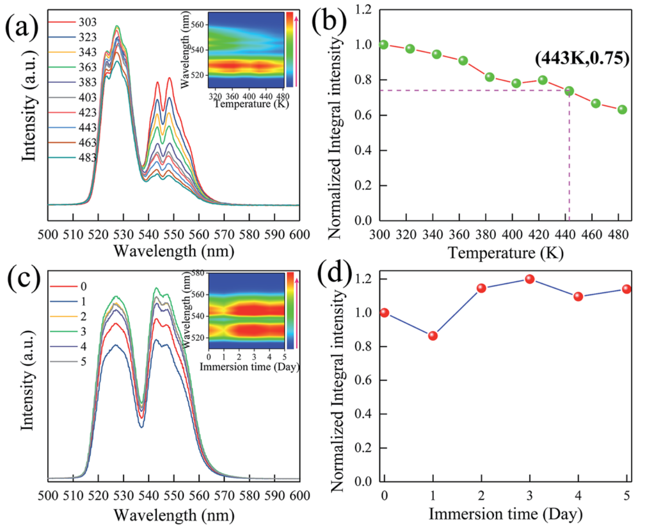

Fig. 5 (a) Thermal quenching behavior of PL emission spectra of LiLaMgWO$_6$:0.01Er^{3+} phosphors under 378.25 nm excitation in the temperature range from 303 to 483 K. Inset: the visual thermal quenching behavior. (b) Temperature-dependent normalized integrated PL intensities. (c) PL spectra of pristine LiLaMgWO$_6$:0.01Er^{3+} and samples with different immersion times. Inset: the corresponding visual chemical stability behavior. (d) The dependence of normalized integrated PL intensities as a function of immersion time.

chemical stability (inset in Fig. 5c). Furthermore, the integrated intensity of emission does not show obvious change even after water treatment for 5 days, suggesting that the developed phosphors are a chemically stable material. Based on these results, we conclude that our prepared sample possesses excellent thermal and chemical stability, prompting its practical application.

Ratiometric temperature sensing

To realize a ratiometric thermometer using the different temperature responses of Er^{3+} emission, the phosphor LiLaMgWO$_6$:0.01Er^{3+} is chosen as a representative. In view of emission intensity, the intensity ratio changes greatly. In detail, as in Fig. 5a, the intensity of Er^{3+} emission at 527 nm first increases and then decreases and the emission band at 544 nm substantially decreases. These results further indicate that the population between the $^2H_{11/2}$ and $^4S_{3/2}$ levels can be redistributed at elevated temperature and the ($^2H_{11/2}$, $^4S_{3/2}$) levels are thermally coupled energy levels. Thus, we conclude that our prepared phosphors can provide good temperature sensing property and considerable performance. Fig. 6a shows the corresponding normalized PL results at about 544 nm under different temperature conditions.

It has been reported that the relative population of the ($^2H_{11/2}$, $^4S_{3/2}$) thermally coupled energy levels follows the Boltzmann distribution.[26] Fig. 6b depicts the FIR values as a function of temperature. It can be found that FIR values increase with rising temperature, obtaining the maximum value (4.78) at 483 K. A linear relationship between FIR and temperature with a correlation coefficient (R^2) of 0.99901 can be obtained using the following expression:[27]

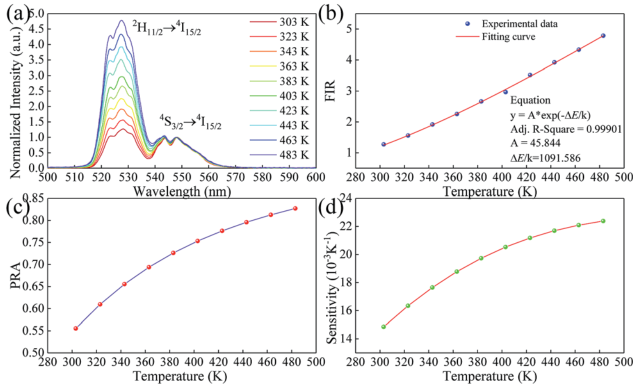

Fig. 6 (a) Normalized green emission spectra of LiLaMgWO$_6$:0.01Er^{3+} phosphor at various temperatures. (b) FIR value related to temperature. (c) Temperature-dependent PRA as a function of temperature. (d) Sensor sensitivity as a function of temperature in the range of 303–483 K for LiLaMgWO$_6$:0.01Er^{3+} phosphor.

$$\mathrm{FIR} = \frac{I_\mathrm{H}}{I_\mathrm{S}} = A\,\mathrm{e}^{-\frac{\Delta E}{kT}}. \tag{4}$$

In the above equation, I_H represents the integrated emission intensities for the $^2H_{11/2} \to {}^4I_{15/2}$ (511–537 nm) transitions of Er^{3+} ions, while I_S denotes the integrated emission intensities for the $^4S_{3/2} \to {}^4I_{15/2}$ (537–583 nm) transitions of Er^{3+} ions. A is constant and ΔE is the energy gap of the thermally coupled energy levels. T is the temperature and k refers to the Boltzmann constant. In addition, according to eqn (4), the fitted experimental data give $\frac{\Delta E}{k}$ and A values of 1091.586 and 45.844, respectively. Based on this, the energy gap of the thermally coupled energy levels of $^2H_{11/2}$ and $^4S_{3/2}$ is defined as about 753.2 cm^{-1}.

Furthermore, the temperature-dependent population redistribution ability (PRA) was used, as follows:[28]

$$\mathrm{PRA} = \frac{I_\mathrm{U}}{I_\mathrm{U} + I_\mathrm{L}} = \frac{I_\mathrm{H}}{I_\mathrm{H} + I_\mathrm{S}} \tag{5}$$

In the above equation, I_U and I_L represent the integrated emission intensity, from the upper and lower excited levels, respectively, to the ground state. Combined with eqn (5), the PRA can be defined as:

$$\mathrm{PRA} = \frac{A}{A + \mathrm{e}^{\frac{\Delta E}{kT}}}. \tag{6}$$

The calculated result is demonstrated in Fig. 6c. PRA is largely influenced by temperature. Increasing the temperature enhances the value of PRA from 0.555 to 0.827. This result supports the conclusion that the population between thermally coupled energy levels of $^2H_{11/2}$ and $^4S_{3/2}$ is strongly dependent on the temperature surrounding the samples. Thus, it can be expected that our prepared LiLaMgWO$_6$:0.01Er^{3+} materials have good potential application in non-contact optical temperature sensors with high sensitivity.

For this purpose, we analyzed the sensor sensitivity, which can be defined as the rate of FIR as a function of temperature (T). The corresponding equation is as follows:[29]

$$S = \frac{\mathrm{d(FIR)}}{\mathrm{d}T} = \mathrm{FIR} \times \frac{\Delta E}{kT^2}. \tag{7}$$

As shown in Fig. 6d, along with increasing temperature, the value of sensitivity enhanced greatly, achieving the maximum around 0.022384 K^{-1} at 483 K. In addition, compared with previously developed temperature sensors (Table 1), our prepared materials show two advantages: one is the accuracy of temperature measurement induced by higher sensitivity. The other is stronger fluorescence intensity, which can effectively resist the interference of the environment and is further conducive to signal detection and collection. The high sensitivity is due to the absorption of the $\mathrm{WO_6}^{6-}$ group and the stable crystal environment of Er^{3+}.

EL performance of fabricated LED device

The quantum efficiency and absorption efficiency are essential parameters for determining the applicability of the prepared phosphors for light emitting diodes. The quantum efficiency and absorption efficiency at 378 nm excitation were measured to be 4.003% and 13.77%, respectively. The internal quantum efficiency (IQE) was found to be 29.07%. Using the PL results as preconditions, we placed the phosphor in a solid-state lighting application. A green emitting LED device was prepared by integrating an InGaN NUV chip (~385 nm) and the $\mathrm{LiLaMgWO_6{:}0.01Er^{3+}}$ materials. Under the forward bias current of 100 mA, the EL spectrum of the fabricated green-emitting LED device was recorded, as shown in Fig. 7a. According to the results, it is clear that the EL spectrum was composed of three emission regions. The emission band located at approximately 385 nm was assigned to the centre wavelength of the NUV chip. The two green emitting peaks centred at 527 and 544 nm belong to the $^2\mathrm{H}_{11/2} \rightarrow {}^4\mathrm{I}_{15/2}$ and $^4\mathrm{S}_{3/2} \rightarrow {}^4\mathrm{I}_{15/2}$ transitions, respectively, of Er^{3+} ions. The other weak peaks around 660 nm are related to the $^4\mathrm{F}_{9/2} \rightarrow {}^4\mathrm{I}_{15/2}$ transitions of Er^{3+} ions, which can be ascribed to the effective cross relaxation (CR) and energy transfer processes among adjacent Er^{3+} ions. As expected, the constructed LED device shows a bright green light which can be observed by the naked eye (Fig. 7b). The CIE chromaticity diagram of the prepared green LED is (0.2699, 0.6670). Simultaneously, the obtained optical parameter of correlated color temperature (CCT) is 6827 K. These results prove the good potential of our developed $\mathrm{LiLaMgWO_6}$-based phosphors with excellent emitting property for application in solid-state lighting.

Table 1 Temperature sensing performance of Er^{3+}-activated luminescent materials

Compounds	Temperature range (K)	$\Delta E/k$	Sensitivity	Ref.
$\mathrm{NaYb_2F_7{:}Er^{3+}}$	300–770	1226	0.0030	22
$\mathrm{La_2MoO_6{:}Er^{3+}}$	303–463	1105	0.0097	28
$\mathrm{Y_2O_3{:}1\%Er^{3+}, 0.5\%Ho^{3+}}$	24–457	914	0.0057	30
$\mathrm{CaZnOS{:}Er^{3+}}$	303–603	1178	0.0033	31
$\mathrm{Bi_4Ti_3O_{12}{:}Er^{3+}}$	115–490	1123	0.0043	32
$\mathrm{(Ba_{0.4}Ca_{0.6})TiO_3{:}Er^{3+}}$	103–543	1009	0.0033	33
$\mathrm{NaGd(MoO_4)_2}$	298–593	970	0.0161	34
$\mathrm{La_2O_3{:}Er^{3+}}$	303–573	942	0.0046	35
$\mathrm{Sr_2Gd_8(SiO_4)_6O_2{:}Er^{3+}}$	303–483	958	0.0034	36
$\mathrm{NaY(WO_4)_2{:}Er^{3+}}$	30–300	1509	0.0050	37
$\mathrm{LiLaMgWO_6{:}Er^{3+}}$	303–483	1092	0.0224	This work

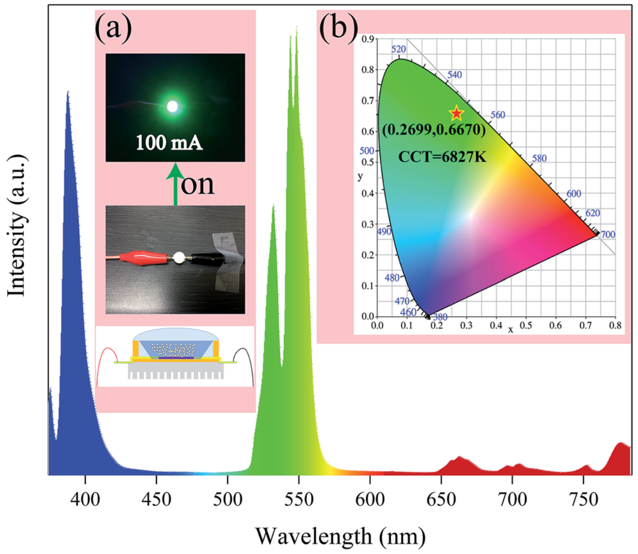

Fig. 7 EL spectrum of the fabricated green-emitting LED device. (a) Digital images of the fabricated device without and with power input. (b) CIE chromaticity diagram of the $\mathrm{LiLaMgWO_6{:}0.01Er^{3+}}$ materials.

Conclusions

In summary, we developed efficient bifunctional Er^{3+}-activated $\mathrm{LiLaMgWO_6}$ phosphors. The physicochemical properties of the samples were detected by XRD, UV-vis absorption spectra, XPS, *etc.*, suggesting that the Er^{3+} ions were doped in the host lattice. The optimal doping concentration of Er^{3+} ions in the $\mathrm{LiLaMgWO_6}$ host material was determined to be 1 mol% and the main concentration quenching mechanism was energy transfer among the nearest neighbor ions. The temperature-dependent and water-treated PL emission spectra of the optimized phosphors revealed that the studied phosphors possessed excellent thermal and chemical stability. The resultant phosphors could be efficiently excited by a commercial NUV chip and emitted visibly bright green light. With high luminescence intensity, a good index relationship between FIR and temperature ($R^2 > 0.999$), wide sensing range (303–483 K) and high sensitivity (2.24% K^{-1}), our developed phosphors could be good candidates for high-sensitivity optical thermometry in a high-temperature environment. Such a system not only optimizes the performance for solid light emitting but also provides an excellent platform for designing novel temperature sensors.

Conflicts of interest

There are no conflicts to declare.

Acknowledgements

This research was supported by the Basic Science Research Program through the National Research Foundation of Korea (NRF) funded by the Ministry of Science, ICT and Future Planning (No. 2018R1A2B6005179). The $LiLaMgWO_6$:$x$$Er^{3+}$ phosphors were supplied by the Functional Phosphor Bank at Pukyong National University (2017M3A9B8069470).

Notes and references

1 Y. Chen, Y.-C. Wang, Y. Zhang, H. Zou, Z. Lin, G. Zhang, C. Zou and Z. L. Wang, *Adv. Energy Mater.*, 2018, **8**, 1802159.
2 F. Kong, X. Fan, A. Kong, Z. Zhou, X. Zhang and Y. Shan, *Adv. Funct. Mater.*, 2018, 1803973.
3 J.-f. Feng, S.-y. Gao, T.-f. Liu, J. Shi and R. Cao, *ACS Appl. Mater. Interfaces*, 2018, **10**, 6014–6023.
4 L. Marciniak, K. Prorok and A. Bednarkiewicz, *J. Mater. Chem. C*, 2017, **5**, 7890–7897.
5 E. J. McLaurin, V. A. Vlaskin and D. R. Gamelin, *J. Am. Chem. Soc.*, 2011, **133**, 14978–14980.
6 D. Dutzler, M. Seibald, D. Baumann and H. Huppertz, *Angew. Chem., Int. Ed.*, 2018, **57**, 13676–13680.
7 M.-H. Fang, J. L. Leaño and R.-S. Liu, *ACS Energy Lett.*, 2018, **3**, 2573–2586.
8 M. Zhao, H. Liao, L. Ning, Q. Zhang, Q. Liu and Z. Xia, *Adv. Mater.*, 2018, **30**, 1802489.
9 A. M. Kaczmarek, *J. Mater. Chem. C*, 2018, **6**, 5916–5925.
10 P. Kayser, S. Injac, B. J. Kennedy, T. Vogt, M. Avdeev, H. E. Maynard-Casely and Z. Zhang, *Inorg. Chem.*, 2017, **56**, 6565–6575.
11 M.-H. Fang, W.-L. Wu, Y. Jin, T. Lesniewski, S. Mahlik, M. Grinberg, M. G. Brik, A. M. Srivastava, C.-Y. Chiang, W. Zhou, D. Jeong, S. H. Kim, G. Leniec, S. M. Kaczmarek, H.-S. Sheu and R.-S. Liu, *Angew. Chem., Int. Ed.*, 2018, **57**, 1797–1801.
12 B. Zhao, L. Zhang, D. Zhen, S. Yoo, Y. Ding, D. Chen, Y. Chen, Q. Zhang, B. Doyle, X. Xiong and M. Liu, *Nat. Commun.*, 2017, **8**, 14586.
13 B. Weng, C. R. Grice, J. Ge, T. Poudel, X. Deng and Y. Yan, *Adv. Energy Mater.*, 2018, **8**, 1701655.
14 S. C. Lal, V. Lalan and S. Ganesanpotti, *Inorg. Chem.*, 2018, **57**, 6226–6236.
15 M. C. Knapp and P. M. Woodward, *J. Solid State Chem.*, 2006, **179**, 1076–1085.
16 K. Singh, W. H. Kan, B. Patton, A. Huq and V. Thangadurai, *Inorg. Chem.*, 2018, **57**, 2609–2619.
17 K.-z. Du, W. Meng, X. Wang, Y. Yan and D. B. Mitzi, *Angew. Chem., Int. Ed.*, 2017, **56**, 8158–8162.
18 B. A. Connor, L. Leppert, M. D. Smith, J. B. Neaton and H. I. Karunadasa, *J. Am. Chem. Soc.*, 2018, **140**, 5235–5240.
19 A. Grimaud, K. J. May, C. E. Carlton, Y.-L. Lee, M. Risch, W. T. Hong, J. Zhou and Y. Shao-Horn, *Nat. Commun.*, 2013, **4**, 2439.
20 J. Luo, X. Wang, S. Li, J. Liu, Y. Guo, G. Niu, L. Yao, Y. Fu, L. Gao, Q. Dong, C. Zhao, M. Leng, F. Ma, W. Liang, L. Wang, S. Jin, J. Han, L. Zhang, J. Etheridge, J. Wang, Y. Yan, E. H. Sargent and J. Tang, *Nature*, 2018, **563**, 541–545.
21 M.-R. Li, E. E. McCabe, P. W. Stephens, M. Croft, L. Collins, S. V. Kalinin, Z. Deng, M. Retuerto, A. Sen Gupta, H. Padmanabhan, V. Gopalan, C. P. Grams, J. Hemberger, F. Orlandi, P. Manuel, W.-M. Li, C.-Q. Jin, D. Walker and M. Greenblatt, *Nat. Commun.*, 2017, **8**, 2037.
22 F. Hu, J. Cao, X. Wei, X. Li, J. Cai, H. Guo, Y. Chen, C.-K. Duan and M. Yin, *J. Mater. Chem. C*, 2016, **4**, 9976–9985.
23 D. L. Dexter and J. H. Schulman, *J. Chem. Phys.*, 1954, **22**, 1063–1070.
24 D. L. Dexter, *J. Chem. Phys.*, 1953, **21**, 836–850.
25 J. P. Perdew, K. Burke and M. Ernzerhof, *Phys. Rev. Lett.*, 1996, **77**, 3865–3868.
26 B. Dong, B. Cao, Y. He, Z. Liu, Z. Li and Z. Feng, *Adv. Mater.*, 2012, **24**, 1987–1993.
27 L. H. Fischer, G. S. Harms and O. S. Wolfbeis, *Angew. Chem., Int. Ed.*, 2011, **50**, 4546–4551.
28 P. Du and J. S. Yu, *Chem. Eng. J.*, 2017, **327**, 109–119.
29 P. Du and J. S. Yu, *Ind. Eng. Chem. Res.*, 2018, **57**, 13077–13086.
30 X. Wang, Y. Wang, J. Marques-Hueso and X. Yan, *Sci. Rep.*, 2017, **7**, 758.
31 H. Zhang, D. Peng, W. Wang, L. Dong and C. Pan, *J. Mater. Chem. C*, 2015, **119**, 28136–28142.
32 T. Wei, T. B. Zhang, Y. J. Ma, Y. F. Xie, C. Z. Zhao, F. M. Yang, H. Y. Xiao and Y. Zhao, *RSC Adv.*, 2016, **6**, 7643–7652.
33 X. Chai, J. Li, X. Wang, H. Zhao, Y. Li and X. Yao, *J. Mater. Sci. Eng. B*, 2015, **201**, 23–28.
34 W. Bi, Q. Meng, W. Sun and S. Lu, *Ceram. Int.*, 2017, **43**, 1460–1465.
35 G. Chen, R. Lei, S. Xu, H. Wang, S. Zhao, F. Huang and Y. Tian, *J. Rare Earths*, 2018, **36**, 119–124.
36 G. S. R. Raju, E. Pavitra, G. M. Rao, T.-J. Jeon, S.-W. Jeon, Y. S. Huh and Y.-K. Han, *J. Alloys Compd.*, 2018, **756**, 82–92.
37 H. Yao, H. Shen, Q. Tang, J. Peng and R. Liu, *Mater. Chem. Phys.*, 2018, **219**, 361–367.